Palaeogeography, Palaeoclimatology, Palaeoecology 610 (2023) 111332

Contents lists available at ScienceDirect

Palaeogeography, Palaeoclimatology, Palaeoecology

journal homepage: www.elsevier.com/locate/palaeo

Environmental shifts in and around Lake Pannon during the Tortonian Thermal Maximum based on a multi-proxy record from the Vienna Basin (Austria, Late Miocene, Tortonian)

Mathias Harzhauser [a,b,*], Mandana Peresson [c], Christian Benold [c], Oleg Mandic [a], Stjepan Ćorić [c], Gert J. De Lange [d]

[a] Geological-Paleontological Department, Natural History Museum Vienna, Burgring 7, 1010 Vienna, Austria
[b] Institute of Earth Sciences, University Graz, Heinrichstraße 26, 8010 Graz, Austria
[c] Geological Survey Austria, Neulinggasse 38, 1030 Vienna, Austria
[d] Department of Earth Sciences-Geochemistry, Faculty of Geosciences, Utrecht University, Utrecht, the Netherlands

ARTICLE INFO

Editor: H. Falcon-Lang

Keywords:
Miocene
Tortonian
Lake Pannon
Anoxia
Clay minerals
XRF-analysis

ABSTRACT

The Neogene Lake Pannon was the largest lake that ever existed in Europe. It attained its greatest extent during the Tortonian Thermal Maximum. For the first time, results from a detailed lake record documenting about 85 kyr of Late Miocene time in a continuously recovered, 60-m-long, clay-rich core of Lake Pannon are reported. This record includes the transition from the lake's maximum transgression into its highstand at around 10.4 Ma. The environmental development of Lake Pannon during its maximum extent is interpreted based on integrated paleontological, sedimentological, mineralogical and geochemical data. The maximum extent coincided with stable sedimentation of clay, little influx from the hinterland, low surface productivity and severe bottom-water anoxia. The clay mineralogy of the lower part of the core points to prevailing chemical weathering based on the illite/smectite ratios. Distinct Fe, Mn and Ba enrichments are interpreted to have formed close to sulfate-methane transition zones during the maximum flooding. The highstand phase was marked by rapid environmental shifts with frequent phases of well-oxygenated bottom waters. These phases are reflected by rich benthic communities including stenohaline tunicates. The increased input of detritic kaolinite suggests a shift towards physical weathering and higher precipitation coinciding with a shift in the provenance of clay minerals.

Increasing amounts of nutrients stimulated surface water productivity and nannoplankton blooms. Despite the offshore position of the core at ~8 km from the mountainous ranges of the Alps, strong fluvial input is reflected from 32.5 to 30.3 m by coarser sediment and the occurrence of terrestrial and freshwater molluscs. The Rhenodanubian Flysch Unit was the main source of the siliciclastics of the core and was drained by the Paleo-Wien river. Drainage from the Calcareous Alps was limited to an exceptionally strong fluvial event and related deposits, which documents the presence of a second river in the southwest, which might represent the Paleo-Liesing.

The dominance of smectite throughout the core suggests a temperate climate with distinct seasonality during the Tortonian Thermal Maximum. In view of the autochthonous ascidian sclerites in three samples, and assuming generally similar ecological requirements for both Pannonian and modern tunicates, we conclude a polyhaline salinity for Lake Pannon around 10.4 Ma.

1. Introduction

Lake Pannon formed within the Pannonian basins complex after a glacio-eustatic sea-level drop at 11.6 Ma, causing the final disintegration of the central and south-eastern European Paratethys Sea (Kováč et al., 1998, 2017; Magyar et al., 1999; Harzhauser et al., 2004; Harzhauser and Mandic, 2008). Its evolution coincided with the Tortonian Thermal Maximum, which was a global warming event (Westerhold et al., 2020).

* Corresponding author at: Geological-Paleontological Department, Natural History Museum Vienna, Burgring 7, 1010 Vienna, Austria.
E-mail addresses: mathias.harzhauser@nhm-wien.ac.at (M. Harzhauser), mandana.peresson@geologie.ac.at (M. Peresson), christian.benold@geologie.ac.at (C. Benold), oleg-mandic@nhm-wien.ac.at (O. Mandic), stjepan.coric@geologie.ac.at (S. Ćorić), g.j.delange@uu.nl (G.J. De Lange).

https://doi.org/10.1016/j.palaeo.2022.111332
Received 6 October 2022; Received in revised form 22 November 2022; Accepted 22 November 2022
Available online 26 November 2022

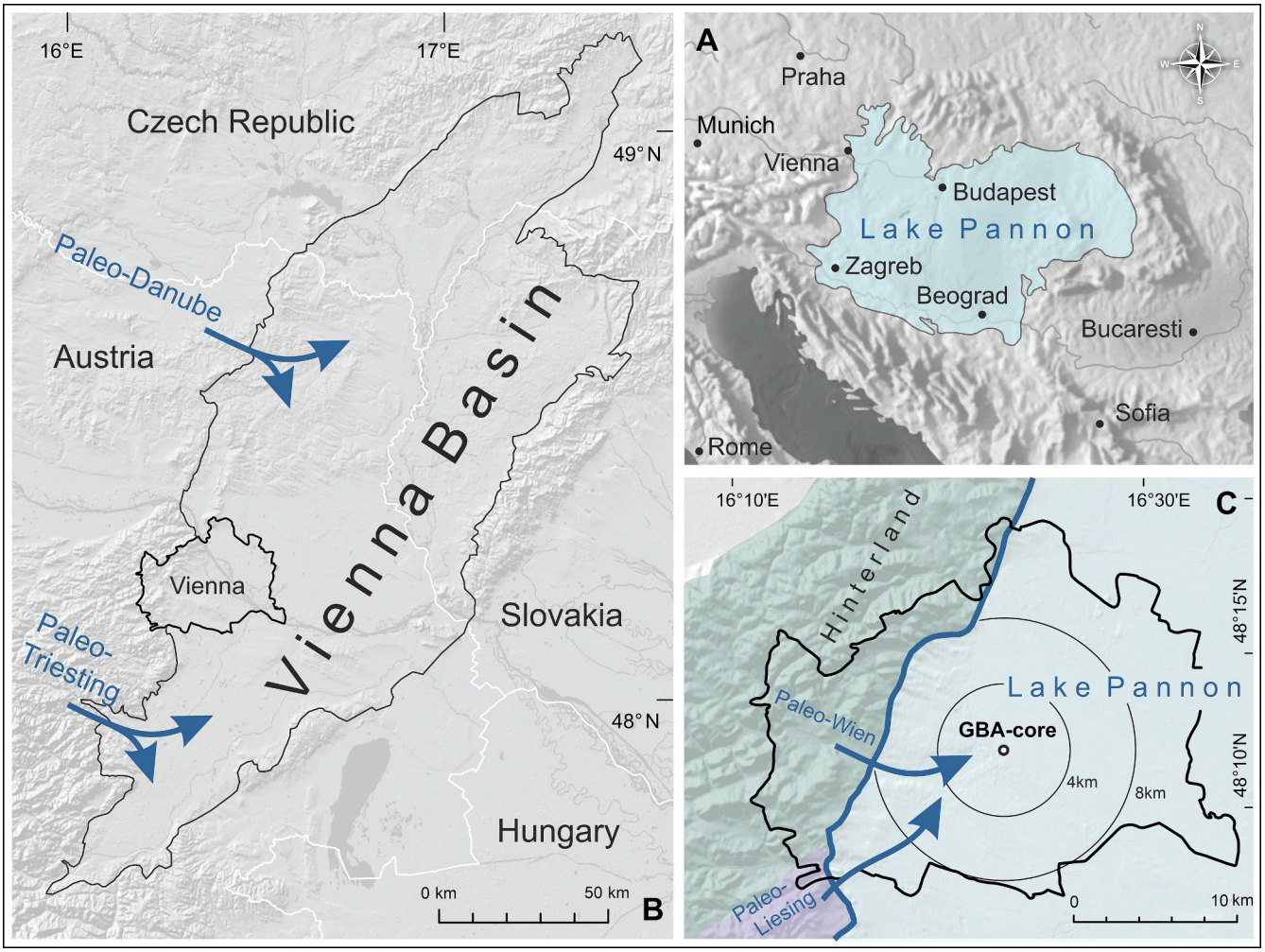

Fig. 1. A. Maximum extent of Lake Pannon around 10.5–10.0 Ma (after Magyar et al., 1999; Harzhauser and Mandic, 2008). B. Outline of the Vienna Basin and position of two major delta complexes entering the basin during the late Miocene (Harzhauser et al., 2004; Wessely, 2006; Borzi et al., 2022). C. Position of the GBA-core within the City of Vienna (black outline) relative to the Alpine hinterland. Green: siliciclastic deposits of the Rhenodanubian Flysch Unit; purple: limestones and dolostones of the Calcareous Alps. Blue arrows: position of the hypothetical deltas of the Paleo-Wien and Paleo-Liesing rivers. (For interpretation of the references to colour in this figure legend, the reader is referred to the web version of this article.)

In a regional context, the Tortonian Thermal Maximum resulted in a phase of increased precipitation, termed "Late Miocene washhouse climate" by Böhme et al. (2008). The lake was outstanding in its size, being the largest that ever existed in Europe (Neubauer et al., 2016a). It attained its maximum extent between 10.5 and 10.0 Ma (Magyar et al., 1999) and covered an area of c. 233,500 km^2 (Neubauer et al., 2016a) (Fig. 1A). This size corresponds roughly to two thirds of the modern Caspian Sea (~371,000 km^2) and represents more than half the size of the modern Black Sea (~435,000 km^2). The time slice we focus on in this study represents this phase of maximum lake size.

We analyzed a 60-m-long core, taken within the City of Vienna (Austria) (GBA-core). Using integrated paleontological, sedimentological, mineralogical and geochemical data, we interpret the environmental development of Lake Pannon during its maximum extent at ~10.4 Ma and during the subsequent highstand.

In coastal sublittoral regions, the bottom water of Lake Pannon was well oxygenized down to about 90 m water depth, which is even below storm wave base (Cziczer et al., 2009). Slightly deeper sublittoral regions, however, were characterized by low oxygen conditions, which were only periodically interrupted by increased bottom water oxygenation on centennial to millennial scales, as indicated by rapid but short-lived settlements by dreissenid bivalves (Harzhauser et al., 2013). In its central parts, Lake Pannon attained a water depth of several hundred meters, where euxinic conditions became established (Magyar et al., 1999; Harzhauser and Mandic, 2008; Magyar, 2021). Severe anoxia below the sediment surface led to the formation of iron-sulfides, which partly can be linked to sulphate-driven anaerobic oxidation of methane (Harzhauser et al., 2018). The sharp chemocline is also reflected by a sudden impoverishment of the mollusc fauna with depth (Magyar, 1995, 2021).

Two major delta systems entered the Vienna Basin during the Late Miocene (Fig. 1B). The Paleo-Danube delta in the northern Vienna Basin at about 40 km distance to the GBA-core and the Paleo-Triesting in the southern Vienna Basin about 30 km from the GBA-core (Harzhauser et al., 2004; Wessely, 2006). Both delta bodies developed mainly during the early Pannonian (Borzi et al., 2022) and had retreated during the maximum transgression of Lake Pannon (Borzi et al., 2022; Harzhauser et al., 2022). Therefore, these deltas were rather distant and contributed only minimally to the deposition of material at the studied core-site.

After about 10.0 Ma the lake shrank in size, especially due to the stepwise progradation of the Paleo-Danube delta from NW to SE (Magyar et al., 1999; Magyar et al., 2013; Sztanó et al., 2015; Magyar, 2021). This phase is not covered by the investigated core. Finally, Lake Pannon vanished during the Pliocene after seven million years of existence (Neubauer et al., 2016b; Magyar, 2021).

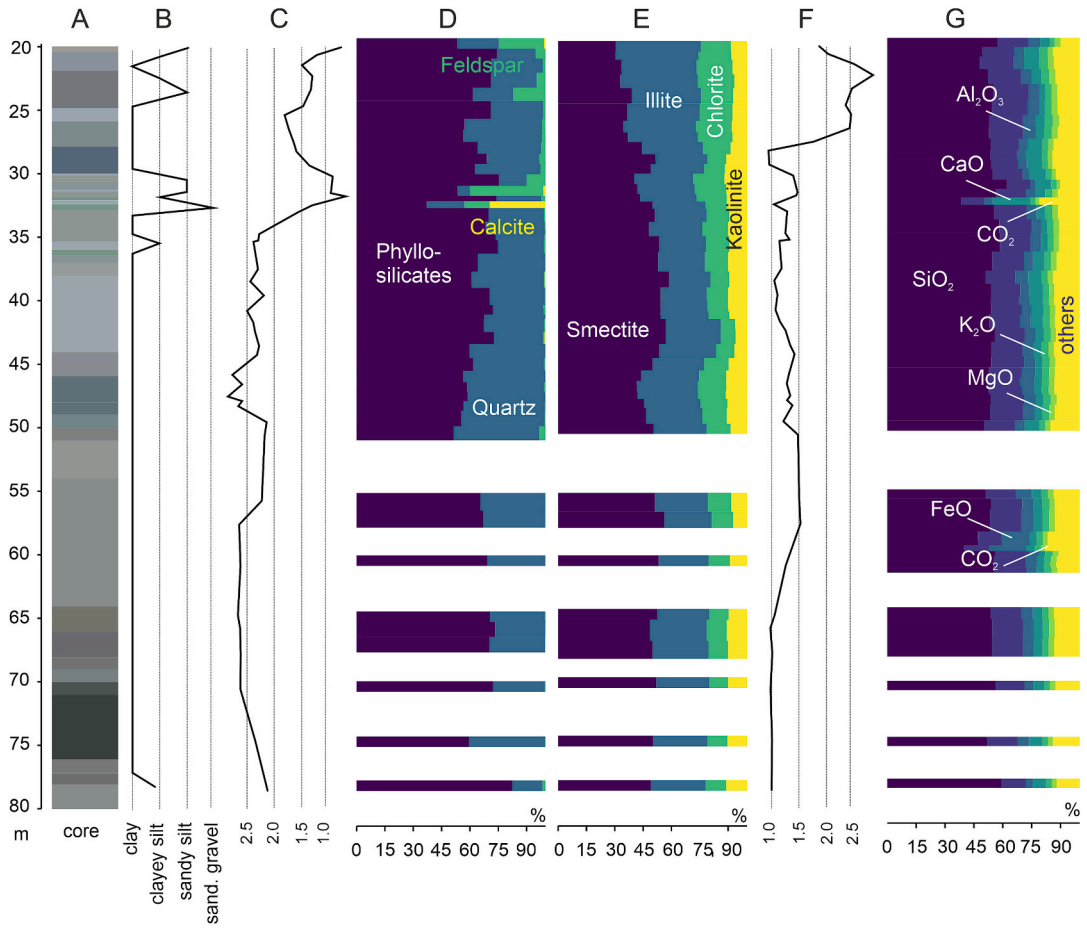

Fig. 2. Log of the GBA-core indicating colour (A), sedimentology (B), ratio between clay-silt and sand (C), mineralogy (D), clay mineralogy (E), illite/smectite ratio (F) and oxides (G).

1.1. Geographical setting and stratigraphy

In 2019, an 80-m-deep well was drilled in the garden of the Geological Survey of Austria located in the 3rd district close to the city center of Vienna (48°12′2.45″N, 16°23′6.35″E) as a geothermal and geophysical test site (Fig. 1C). Tectonically, the drilling site is located in the western part of the Vienna Basin. Beneath an Anthropocene layer (0–2.75 m), a Pleistocene succession follows down to 14.2 m, comprising loess and fluvial subangular gravel from the Rhenodanubian Flysch Unit (RFU) of the Vienna Woods, this is intercalated by alluvial redeposited loess and well-rounded gravels from the Danube River. This lithological succession is typical for the so-called 'Stadtterrasse' (Riss glaciation) (Küpper, 1965) corresponding to 'Niveau 5′ of Grupe et al. (2021). This is followed downcore by blue-grey clays and silts of the middle Pannonian Bzenec Formation (= lower Tortonian) (Harzhauser et al., 2004), which were cored down to the final depth of 80 m. Within the GBA-core (GBA = Geologische Bundesanstalt) the upper part of the Pannonian strata down to 20 m is rich in carbonate and sandstone concretions, indicating strong alteration of the deposits by weathering and pedogenesis during Pleistocene times, when these deposits formed the landscape. Therefore, only the interval from 20 to 80 m is considered here (Fig. 2A). Coeval Pannonian deposits are widespread in the Vienna Basin and are exposed in the south of Vienna in a few partly abandoned clay pits (e.g., Hennersdorf in Kern et al., 2012, 2013).

The mollusc assemblage of the GBA-core comprises the biostratigraphically significant bivalves *Lymnocardium schedelianum* (Fuchs, 1870) (29.75 m), *Congeria subglobosa* Partsch, 1835 (30.15 m) and *Sinucongeria primiformis* (Papp, 1951) (51.5 m) along with the gastropod *Melanopsis vindobonensis* Fuchs, 1870 (31.7 m). This assemblage is indicative of the *Lymnocardium schedelianum* Subzone of Magyar et al. (1999) and corresponds to the Pannonian Zone E of Papp (1951) (see Harzhauser and Mandic, 2004; Harzhauser et al., 2022). Based on the magnetostratigraphic correlation with the long normal chron C5n by Magyar et al. (1999) and astronomically tuned well-logs (Lirer et al., 2009), Harzhauser et al. (2004) and Kern et al. (2012) derived an absolute age of about 10.4 Ma for the deposits considered in this study.

Kern et al. (2012) and Harzhauser et al. (2022) calculated sedimentation rates for the middle Pannonian of the Vienna Basin. The former authors used a correlation of a 6-m-long high-resolution set of geophysical data with high-frequency solar cycles. Alternatively, the latter autors correlated the entire Pannonian sediment stack with the astronomical tuning by Lirer et al. (2009). The resulting sedimentation rates for both are around 0.6–0.7 m/ka for the middle Pannonian. Applying this estimate sets a frame of ~100–85 ka for the deposition of the 60-m-thick GBA-core.

2. Material and methods

The well was fully cored down to 80 m and the core is referred to herein as GBA-core. The cores are stored in wooden boxes of 1 m length and are available for further sampling in the core shed of the Geological Survey of Austria at Erzberg (Styria). Analyses were performed at the Geological Survey Austria and the Natural History Museum Vienna. All samples were dried to constant weight in a drying cabinet. Mollusc shells and pyrite concretions were removed before analysis. Depending on the requirements, the samples were crushed (jaw crusher), sieved (mechanical sieve tower) and ground to analytical fineness in a vibration

mill (grain size <60 μm). The used methods are according to Schroll (1974). The loss on drying and loss on ignition were determined according to ÖNORM L1062 (Österreichisches Normungsinstitut, 1988). The result is the mass of the inert sample, which enables drawing conclusions about the water content and, in combination with the other analytical methods, about the composition of the sample.

Grain size distribution was evaluated using a combination of wet sieving in ½ Phi steps and using a Sedigraph for grain sizes <0.032 mm. The sieve analysis data and the data generated from the Micromeritics SediGraph 5100 were subsequently calculated and displayed with the software program SedPakWin (Reitner et al., 2005). Samples were classified according to Füchtbauer (1959).

Bulk mineralogy of the samples was determined by XRD. For bulk mineral analysis the dried samples were loaded into a sample holder as a randomly oriented powder. Diffraction data were collected with a PANalytical X'Pert Pro Powder Diffractometer (goniometer PW 3050/60), Cu-Ka radiation (40 kV, 40 mA), and PIXel-detector (continuous scans, step size 0.013°, measuring time 10 s/step). The samples were run from 2 to 65°, 2Θ). The semiquantitative mineralogical composition was obtained by the computer program SEIFERT AutoQuan based on the Rietveld method (Taut et al., 1998). We distinguished between quartz, feldspar, calcite, dolomite and phyllosilicates, which together account for 100%.

Clay mineralogy was analyzed by treating the samples with H_2O_2 to remove organic matter and with ultrasonics for further disaggregation. The <2 μm fractions were separated by centrifugation. The clay fractions were saturated with 1 N KCl-solutions and 1 N $MgCl_2$-solutions by shaking for 24 h and subsequently washed in distilled water. Oriented preparations of the <2 μm fractions were achieved by suction of 25 mg clay in suspension on a porous ceramic plate and drying at room temperature. Oriented XRD mounts were then analyzed in the airdried state and exposed to ethylene glycol and dimethyle sulfoxide. The clay samples were run from 2 to 50° 2Θ with the same step and counting time as the bulk samples. Clay minerals were identified according to Moore and Reynolds (1989). Note that values for clay mineralogy per sample refer to the % of phylloscilicates given in the bulk mineralogy. E.g., sample 20.2 m contains 42% phyllosilicates (smectite 10.5%, illite 21.4%, kaolinite 3.4%, chlorite 6.7%). For a meaningful comparison, the total clay mineral content per sample was set to 100%.

The *elemental determination by XRF* was realized with two different instruments and different methods: In the field, a Portable XRF: Thermo Scientific XL3t GOLDD+ XRF Analyser was used directly on freshly exposed sediment with the following specifications: The X-ray tube consists of an Au anode with 50 kV maximum power (at max. 200 μA). The measurement passes through three different filters (high, medium and low) to guarantee the best element-specific excitation energies of the atoms. Nominal Test time is 90 s. A high-resolution semiconductor ensures the detection. A Peltier element provides the cooling at a permanent operating temperature of min. −25 °C (Analyticon Instruments GmbH 2010). 140 samples were measured in the field.

Additionally, 49 samples were selected for preparation (drying, grinding) and laboratory analysis. XRF elemental analysis was carried out on an Epsilon 5 Panalytical spectrometer. Powdered samples (4 g) were processed into press tablets using Hoechst wax C micro powder (0.9 g per tablet) at a pressure of ten bar (Schramm, 2012). These press tablets were subsequently analyzed in the spectrometer. A gadolinium X-ray tube serves as the primary source of radiation. Light-intensive Bragg and Barkla polarizers serve as filters. This enables the detector system to process more fluorescence radiation from the sample elements under investigation. The typical measurement time varied between 100 and 300 s per sample and target. The detection limit is 1 ppm.

Sample resolution: the average XRF sampling distance is 0.43 m (n = 140) for the in-field measurements and 1.2 m for the laboratory analysis. The average sampled interval was around 3 cm; the sample frequency for mineralogical and sedimentological analyses ranged around 0.91 m from 20 to 50 m (n = 33) and increased to 3.1 m in the lower part from 55 to 80 m (n = 9).

Calcareous Nannoplankton: 47 samples were analyzed for Calcareous Nannoplankton. All samples were treated for a few seconds in an ultrasonic bath. Afterwards smear slides were made by drying a few drops of suspension on the object glass and fixed using Canada balsam. All smear slides were investigated with a Leica microscope with 1000-fold magnification.

Ascidians: tunicate spicules were counted during analysis of nannofossil samples.

Plant debris: presence/absence of plant debris is based on analysis of nannofossil samples.

Mollusca: shells of molluscs were documented and collected during the drilling campaign.

Ostracoda: 47 samples were analyzed for ostracods (100 g). All samples were treated with diluted H_2O_2 (12%) and sieved with tap water through a standard set of sieves (500, 250, 125 and 63 μm) and later oven dried at 40 °C. All valves were picked from the residue for quantitative comparisons.

Statistical analyses: to reveal positive or negative correlations between data, we calculated Pearson's correlation coefficient (PCC) with the software PAST version 4.0 (Hammer et al., 2001). A PCC of 1 and − 1 represents full positive or negative correlations, and a value around 0 indicates no correlation at all (Hammer, 2021).

See Supplementary Table 1 for full dataset.

3. Results

3.1. Grain size, sedimentology, mineralogy and clay minerals

Forty-three samples were sedimentologically analyzed (Supplementary Table 1). 76% of the samples represent clay (silt/clay ratio = 2.0, σ = 0.5) followed by 11.6% of clayey silt (silt/clay ratio = 3.6, σ = 1.0). Only four samples contained sandy silt, and a single sample at 32.5 m comprised sandy fine gravel. Thus, the GBA-core is generally characterized by a monotonous succession of massive dark grey and greyish blue-green claysilt with subordinate clayey silt (Figs. 2A–G). The upper part of the core displays a slight coarsening trend, indicated by increasing contributions by sand within the clayey matrix, culminating in interval 32.5 to 30.3 m. Mineralogically, the samples consist of 47.9% phyllosilicates (σ = 8.9), 26.2% quartz (σ = 5.9), 14.4% feldspar (σ = 2.9) and 11.0% carbonate (σ = 4.8) (Fig. 2D). Overall, the composition displays little variation except for a distinct carbonate peak at 32.5 m. Carbonate is represented by dolomite and calcite. The dolomite content ranges around a mean of 7.5% without trends or marked peaks (not plotted). The calcite content of the samples ranges around 3.3% with a distinct peak of 31% at 32.5 m. Calcite and dolomite are not significantly correlated (PCC = -0.37, p = 0.03).

No lamination is developed, and bedding planes are mainly indicated by rare mollusc coquinas. Bioturbation is rare except for the interval from 50 to 55 m. Scattered pyrite concretions of few mm diameter occur throughout the succession but were removed before analysis.

Forty-three samples were analyzed for clay mineral content. Herein, we evaluated the relative weight percentage of smectite, illite, kaolinite and chlorite. In some samples, vermiculite is also present in traces but is not further discussed herein. On average, the samples contain ~47.1% smectite (σ = 10.1), 30.4% illite (σ = 6.9), 13.2% chlorite (σ = 4.4) and 9.4% kaolinite (σ = 2.2) (Fig. 2E). The clay mineral composition is rather constant in the lower and middle parts of the core from 80 m to 30.6 m. Within this interval, the chlorite/kaolinite ratio ranges around 1.2 (σ = 0.25). Starting from 30.6 m upwards, the compositions changes, being expressed by a strong positive trend in the illite/smectite ratio and a strong positive shift of the chlorite/kaolinite ratio. No correlation is evident between clay mineral content and clay-silt grain sizes (PCC = -0.2–0.2). A negative correlation, however, is evident for sand and smectite (PCC = -0.6), whereas sand and illite are positively correlated (PCC = 0.5). Consequently, the positive trend in the illite/smectite and

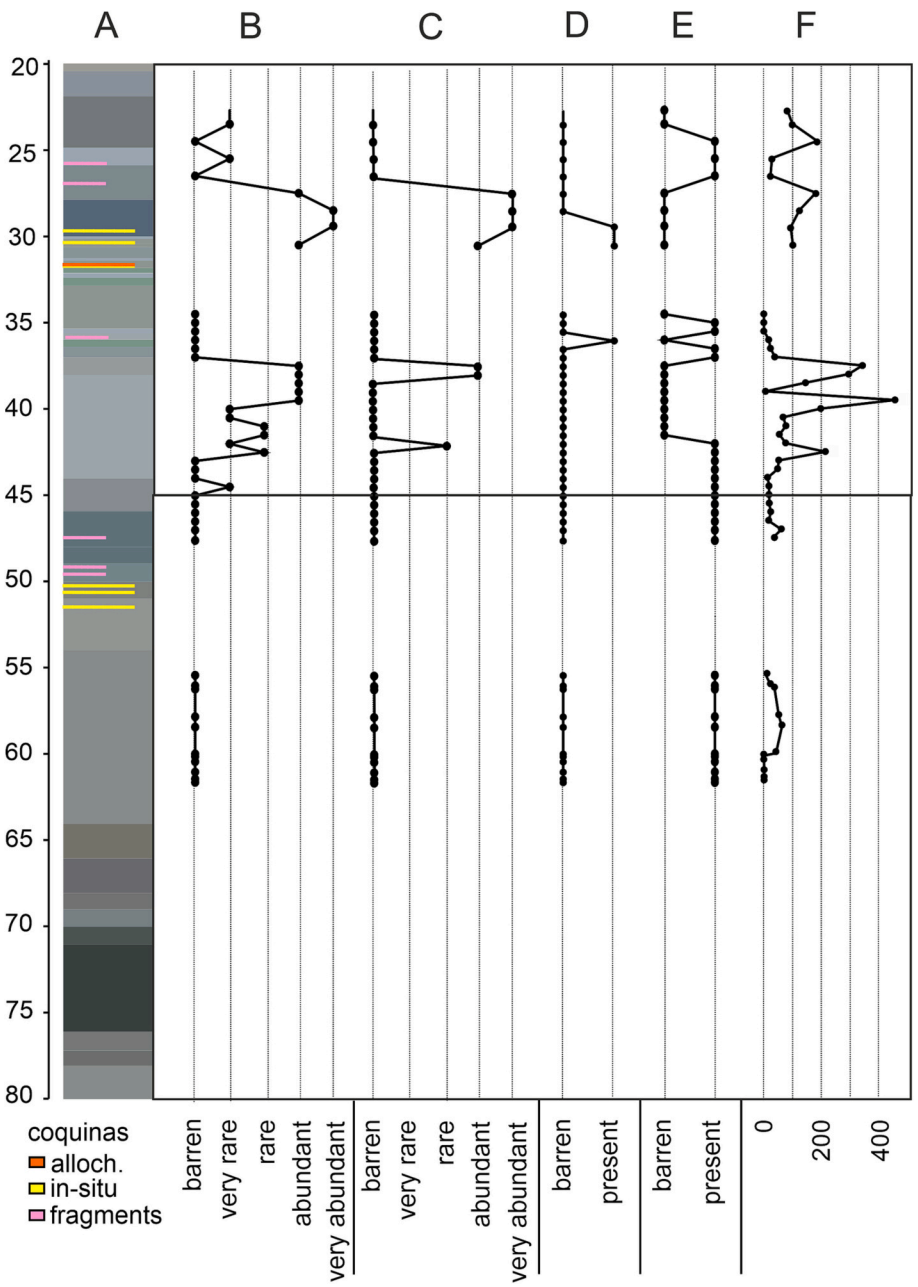

Fig. 3. Log of the GBA-core indicating position of mollusc coquinas (A), amount of allochthonous (B) and autochthonous (C) nannofossils, presence/absence of ascidians (D), plant debris (E) and number of ostracods (F).
Black dots: analyzed samples.

the chlorite/kaolinite ratios is paralleled by a negative trend in the clay-silt/sand ratio (Fig. 2C).

3.2. The fossil record

Autochthonous Calcareous Nannoplankton: The endemic *Noelaerhabdus bozinovicae* is the only autochthonous Pannonian nannoplankton species (Marunteanu, 1997) found in the GBA-core. It was detected in samples 27.3 m, 28.3 m, 29.2 m, 30.3 m, 37.3 m, 37.8 m and 42.3 m (Fig. 3C).

Allochthonous nannofossils: All samples up to 43.3 m are largely barren, followed by an interval from 42.3 m to 37.3 m with frequent nannofossils and a nearly barren interval from 36.8 to 34.8 m (Fig. 3B, Supplementary Table 1). A second peak of nannofossil abundance appears in the interval 30.3 to 27.3 m, followed by moderate abundances above. The nannofossil assemblages are dominated by reworked species from Cretaceous to Eocene formations of the Rhenodanubian Flysch Unit (RFU) containing species such as *Coccolithus formosus*, *Reticulofenestra umbilicus*, *Arkhangelskiella cymbiformis*, *Broinsonia parca*, *Micula staurophora* and *Watznaueria barnesiae*. Few samples also contain rare Miocene species, which were reworked from the surrounding Lower and Middle Miocene deposits, including *Coccolithus miopelagicus* and *Reticulofenestra pseudoumbilicus*.

Ascidians: three samples contained spicules of the didemnid tunicate *Perforocalcinella fusiformis* Bona, 1964. Ascidians are rare in samples 29.2 m and 30.3 m but abundant in sample 35.8 m (Fig. 3D).

Plant debris: indeterminable plant debris was detected during the analysis of nannofossil-samples. Plant debris is abundant in all samples from base to sample 41.8 m and in the intervals from 36.3 to 34.8 m and 26.3–24.3 m. Intervals without detectable plant debris occur from 41.3

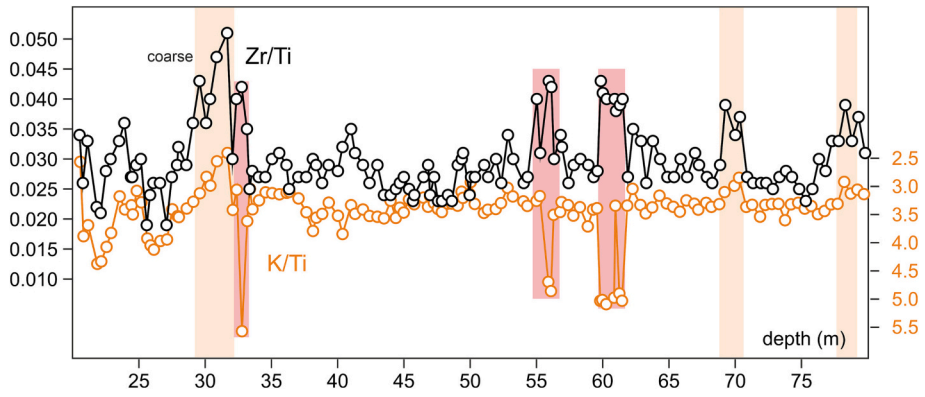

Fig. 4. Zr/Ti and K/Ti ratios. Orange intervals represent phases of increased input of coarse sediment. Samples in red rectangles are influenced by analytical artifacts due to dilution by dominant other phases. (For interpretation of the references to colour in this figure legend, the reader is referred to the web version of this article.)

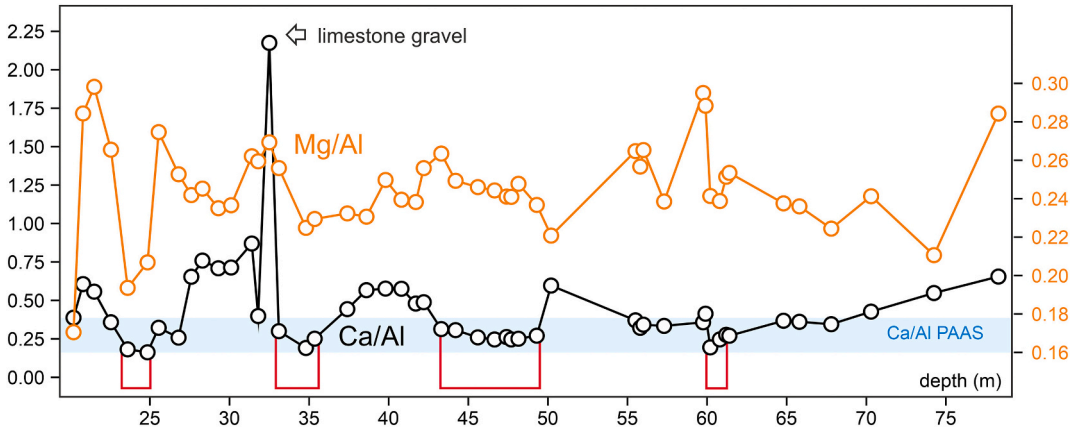

Fig. 5. Mg/Al and Ca/Al ratios. Shaded area: PAAS values for Al-silicates after Taylor and McLennan (1985). Red lines: intervals with reduced input of calcite. (For interpretation of the references to colour in this figure legend, the reader is referred to the web version of this article.)

to 37.3 m and from 34.3 to 27.3 m (Fig. 3E).

Mollusca: are generally rare in the core. Layers with increased amounts of shell fragments occur from 28.0 to 25.6 m and from 50.0 to 47.5 m. Thin pavements of the dreissenid bivalves *Sinucongeria primiformis* and *Coelogonia czjzeki* were detected at 51.5, 50.5 and 50.2 m (Fig. 3A). At 30.7 m, a coquina was detected containing a rich fauna with

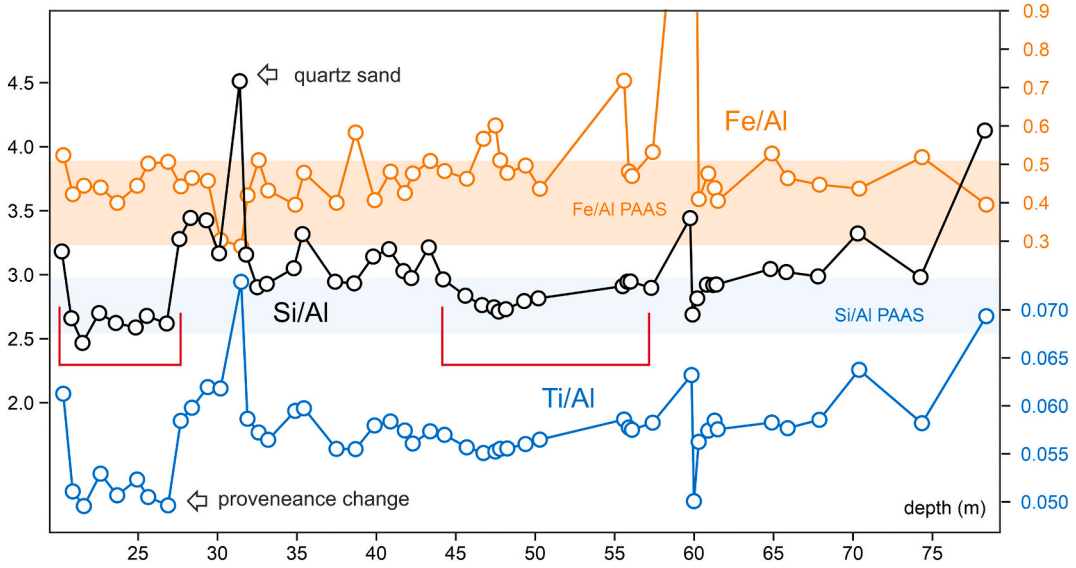

Fig. 6. Fe/Al, Si/Al and Ti/Al ratios (Fe/Al: samples 59.75 (=1.77) and 59.90 (=2.14) not shown). Shaded areas: respective PAAS values for Al-silicates after Taylor and McLennan (1985). Red lines: intervals with reduced input of quartz. (For interpretation of the references to colour in this figure legend, the reader is referred to the web version of this article.)

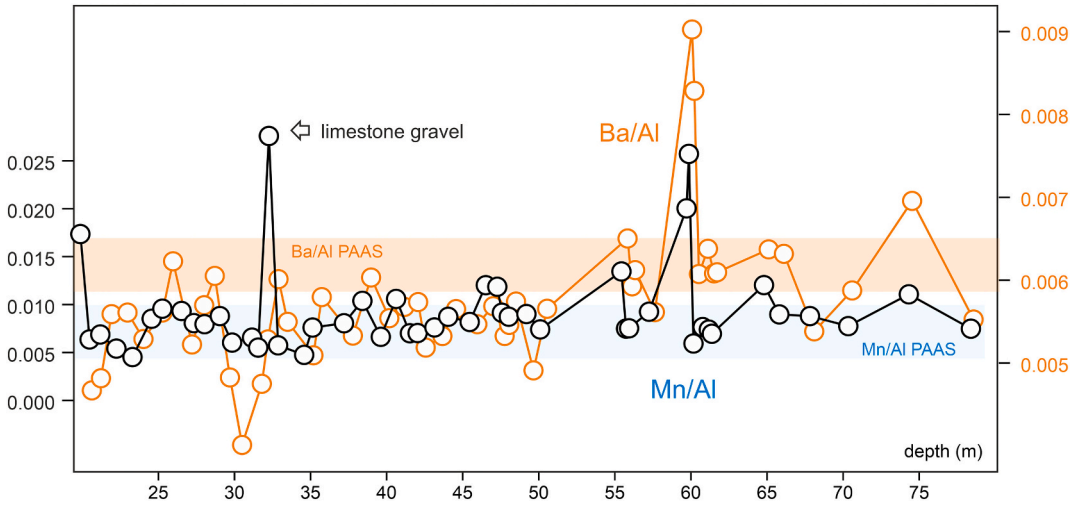

Fig. 7. Ba/Al and Mn/Al ratios. Shaded areas: respective PAAS values for Al-silicates after Taylor and McLennan (1985).

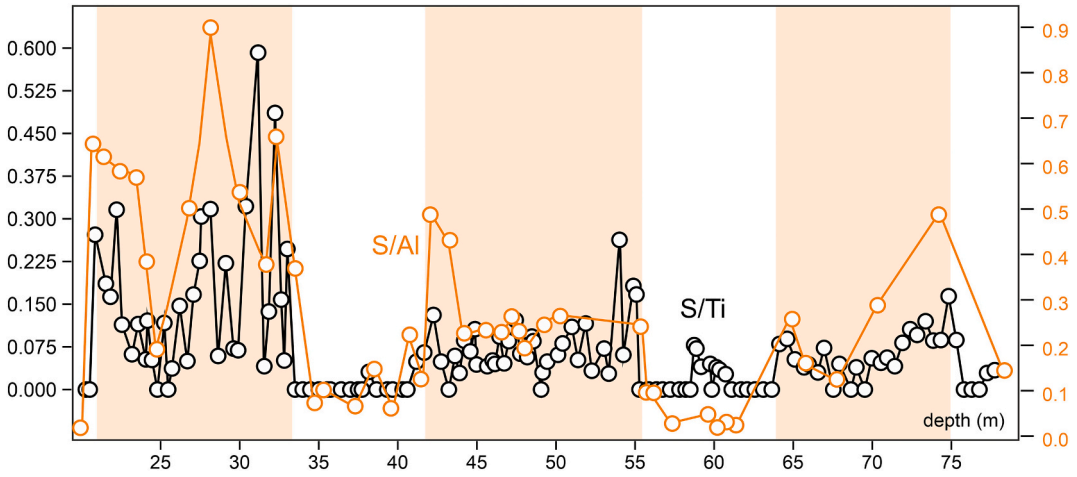

Fig. 8. S/Al and S/Ti ratios. Shaded areas: intervals of initially dysoxic/anoxic conditions.

the gastropods *Melanopsis vindobonensis, Melanopsis pygmaea, Melanopsis rarispina, Goniochilus haidingeri* and *Pseudochloritis* sp. and the bivalves *Unio atavus, Lymnocardium brunnense, Lymnocardium* cf. *carnuntinum, Lymnocardium boeckhi, Monodonta* cf. *voesendorfensis, Parvidacna tinnyeana* and *Parvidacna laevicostata.* In addition, a *Sinucongeria primiformis* pavement is intercalated as well. A further coquina at 30.15 m is characterized by in-situ shells of *Congeria subglobosa* along with *Parvidacna tinnyeana* and *Parvidacna laevicostata*. The uppermost mollusc assemblage was detected at 29.75 m with in-situ occurrences of the cardiid *Lymnocardium schedelianum*.

Ostracoda: The assemblages comprise mainly species of *Cyprideis, Hemicytheria, Lineocypris/Caspiolla, Amplocypris* and *Loxoconcha* and are similar in composition to coeval assemblages described by Harzhauser et al. (2008) from Hennersdorf (Austria). Herein, all species are pooled per sample to achieve the total amount of specimens. The abundance data display considerable variation, ranging from samples without ostracods to peaks of around 450 valves/sample (Fig. 3F). Interval 46.8–34.3 m was sampled in a regular distance of 0.5 m and suggests a succession of intervals with few ostracods (mean = 30 valves/sample) from 46.8 to 42.8 m, passing into an interval with high ostracod frequencies (mean = 175 valves/sample) from 42.5 to 37.3 m, followed from 37.8 to 34.3 m again by an interval of low abundance (mean = 13 valves/sample).

3.3. XRF-data

Two XRF-data sets are available, namely from the field and laboratory measurements. Both data sets are analyzed herein because of the higher resolution of the in-field measurements and the availability of Al and Si from the laboratory set. Although all elements display variations in concentration across the core, the general relation between the elements is fairly constant. Thus, the most abundant elements are Si (~25.0%), Al (~8.4%), Mg (~3.4%), Ca (~3.1%), Fe (~2.8%), K (~1.9%) and Ti (~0.6%) followed with large distance by Mn (~0.05%), Ba (~0.05%) and S (~0.04%) (see Supplementary Table for full data). The element data were normalized with Al and Ti and compared with respective PAAS (Post-Archean Australian Shales) values from Taylor and McLennan, 1985 (Figs. 4–8). Sample 32.5 represents an outlier with very high Ca values of >20%, which is also expressed as a peak in the Ca/Al ratio (Fig. 5). Fe shows a phase of increased values from 61.2 m to 55.8 m with strong peaks at 59. 9 m, 59.75 m and 55.8 m. K displays a phase of higher amplitude fluctuations from 61.2 m to 55.8 m and an interval of low values from 27.6 m to 32.5 m. The Ti-record displays a negative aberration at 32.5 m and a positive peak at 24.5 m (Fig. 4). The negative peaks in Ti and K coincide with the Fe and Ca peaks and are therefore a matter of relative dilution. Sulfur displays strong fluctuations with phases ranging below detection limit alternating with intervals with moderately high concentrations from 65.3 m to 79.8 m, 55.15 m to

41.7 m and from 33.3 m to 20.8 m.

Samples 59.75 and 59.9 m are outliers due to their high FeO and CO_2 contents. X-ray Diffraction (XRD) documented the presence of siderite in these samples. Sample 59.75 m contains 14.6% FeO and 11.2% CO_2 – equivalent to 23.5% $FeCO_3$ and about 2.3% CO_2 – which is bound in other carbonates such as dolomite. Sample 59.9 m has even higher FeO values of 19.1% and 15.1% CO_2, which equals 30.8% $FeCO_3$ with 3.4% of CO_2 bound in other carbonates. Siderite was also detected as an accessory mineral in sample 23.6 m and is absent in other samples. Note that dilution by a dominant phase (e.g. Ca in 32.5 m and Fe at ~59.9, 59.75 m) is reflected by negative peaks in some other elements (see Supplementary Fig. 1).

4. Discussion

4.1. Lake ecology and the biotic signal

The fossils of the GBA-core indicate two different phases of development. The lower part of the core from 80 to 44.8 m is characterized by a lack of ascidians and molluscs and rare or absent ostracods. Simultaneously, the samples are rich in plant debris. Oxygen-depleted bottom water prevailed during deposition of this part of the core. Molluscs appear only in the upper part of this interval, where *Sinugongeria/Coelogonia* pavements at 51.5, 50.5, 50.2, 31.7 and 29.75 m represent autochthonous 'boom-and-bust' populations that developed during short time windows of a few months during increased bottom-water oxygenation (Harzhauser and Mandic, 2004; Harzhauser et al., 2013). Pyrite within the articulated shells indicates that the specimens died off during re-establishment of anoxic conditions followed immediately by microbially mediated pyrite formation (Thiel et al., 2019; Duverger et al., 2020).

The upper part of the core displays a much richer fossil content. Blooms of autochthonous calcareous nannofossils appear in three intervals in the upper core. Endemic Noelaerhabdaceae were frequently described from Pannonian deposits (Ćorić et al., 2017; Ćorić, 2021). Ćorić (2021) discussed a relation between a high abundance of Pannonian nannoplankton and a lake level rise. We do not see any evidence for a lake level rise in this part of the GBA-core and we therefore we assume that the occurrence of Pannonian nannoplankton is related rather to increased surface water productivity due to increased nutrient availability (Peleo-Alampay et al., 1999; Ćorić and Hohenegger, 2008; Auer et al., 2015)).

Fluvial influx becomes evident at 30.7 m by the occurrence of *Melanopsis vindobonensis*, which inhabited deltaic-coastal environments (Neubauer et al., 2013), and by the occurrence of the riverine freshwater mussel *Unio atavus* and the terrestrial gastropod *Pseudochloritis*. After this phase, low oxygen levels developed again, reflected by in-situ occurrences of *Congeria subglobosa* at 30.15 m. This dreissenid species could thrive even in dysoxic conditions due to its assumed chemosymbiosis with sulfur bacteria (Harzhauser and Mandic, 2004). Oxygenated bottom-water conditions became restored around 29.75 m, enabling the establishment of large cardiids.

Blooms of the endemic Paratethyan tunicate *Perforocalcinella fusiformis* have been variously reported from Sarmatian and Pannonian deposits (Schütz et al., 2007; Botka et al., 2019). Tunicates are sessile filter-feeders (Varol and Houghton, 1996). Thus, on the muddy bottom of Lake Pannon, the tunicates might have been attached to bivalve shells, which occur in the same samples. Settlement by ascidians requires abundant oxygen in the water because the animals cannot tolerate hypoxia (Pool et al., 2013). Moreover, ascidians are stenohaline and cannot survive in brackish water conditions (Lambert, 2005). A few species can adapt to lowered salinities below 25 psu (practical salinity unit) but the lethal boundary for extant tunicates seems to range around 22 psu (Vázquez and Young, 1996, 2000; Shenkar and Swalla, 2022).

High-frequency oscillations between ostracod-rich and layers without ostracods are typical for Lake Pannon (Harzhauser et al., 2008; Gross et al., 2011; Kern et al., 2013). These cycles reflect changes in oxygen availability on the lake bottom, and barren samples reflect severe anoxia. Similarly, the presence or absence of plant debris is linked to the availability of oxygen in the sediment. Under oxic conditions, bacterial activity degrades organic material, whereas dysoxic conditions favor preservation of plant tissue (Locatelli, 2014; Hernes et al., 2020).

Thus, the biotic data indicate predominantly hostile conditions with dysoxic oxygen levels at the lake bottom during deposition of the lower part of the core up to 44.8 m, interrupted by short phases of increased bottom-water ventilation between 51.5 and 50.2 m. This is indicated by the high abundance of plant debris, the low number of ostracod specimens and the near absence of molluscs. In the upper part of the core, bottom-water oxygenation increased especially in the interval from 42.5 to 37.3 m, which is reflected by the full degradation of plant debris and the high frequency of ostracods. Nonetheless, conditions were too harsh for settlement by bivalves within this interval. The uppermost part of the core above 37.3 m is characterized by fluctuating bottom-water conditions. Short phases of full oxygenation are reflected by bivalve pavements and the occurrence of tunicates. At that time, surface water productivity was stimulated by increased nutrient input, reflected by blooms of endemic Pannonian nannoplankton. Polyhaline salinity above 22 psu is suggested by the ascidians, which is distinctly higher than the 15 psu estimates in the literature (see Harzhauser et al., 2007a, 2007b).

4.2. Climate-related shifts in grain size and clay mineral composition

The sediment of the GBA-core was mainly derived from the hilly-mountainous Alpine regions, where siliciclastics of the RFU cropped out. Consequently, the RFU was the main source of sediment input during position of the GBA-core. This is especially evident for the upper part of the core, which is rich in reworked Cretaceous-Eocene nannofossils from flysch deposits. An exception is the carbonate gravel at 32.5 m (as revealed by mineralogical analysis). This event documents a short phase of drainage from the Calcareous Alps. The respective river might be some kind of precursor of the modern Liesing river (Paleo-Liesing in Fig. 1C).

Due to the large distance from the shore (about 8 km), increased terrigenous input is reflected mainly by higher contributions of coarse silt. Overall, the lower part of the core up to about 60 m is dominated by clay and silty clay coinciding with a high number of fine phyllosilicates. We interpret this interval as a phase of maximum flooding, which effectively reduced input from the hinterland. In offshore wells of the Vienna Basin (e.g., Eichhorn 1, Aderklaa 40, Fig. 1B), this phase corresponds to the major maximum flooding surface of the middle Pannonian, separating a transgressive fining upwards sequence from the coarsening upwards of the subsequent highstand (Harzhauser et al., 2004, 2022). In these wells, the transgressive part attains about 40 m in thickness (Harzhauser et al., 2004, Fig. 3a). Thus, the interval from 60 to 80 m in the GBA-core covers about half of this transgressive phase.

This stable depositional environment was disturbed by a major runoff event at 32.5 m which marks the onset of a coarsening trend (Figs. 2B–C). The coarsening is mainly linked to input of feldspar (Fig. 2D) and suggests increased fluvial input of silt and sand into the lake. The maximum input was reached in interval 32.5 to 30.3 m, coinciding with the occurrence of sandy gravel. Subsequently, a fining upward trend from 30 to 25 m documents a gradual decrease of coarse input and the re-establishment of calm offshore conditions, although grain size and sedimentology indicate a higher variability, which is also expressed in fluctuating occurrences of detritic dolomite. Therefore, the interval above 32.5 m indicates the beginning retrogradation of the lake due to gradual shoreline progradation during the late lake highstand and the increased influence of the delta of the Paleo-Wien at the GBA-core.

A similar shift is evident in the composition of clay minerals. Clay minerals are derived from weathering of parent rocks from the Rhenodanubian Flysch Unit and/or from paleosols. Their relative abundance in the sediment is strongly related to climatic factors and, therefore, clay

minerals are frequently used as proxies for paleoclimatic interpretations (Singer, 1984; Thiry, 2000). Smectite, which is the dominant clay mineral in the GBA-core, is formed by chemical weathering of volcanic rocks and by neoformation during pedogenesis in soils (Wilson, 1999). In addition, smectite indicates paleoclimates with pronounced seasonality (Singer, 1984). Smectite predominates in sediments if chemical weathering was the dominant clay-producing process in the source area (Singer, 1984). Similarly, kaolinite formation is triggered by chemical weathering of crystalline rocks (Gao et al., 2020). In contrast to smectite, however, kaolinite forms under warm humid climatic conditions with minimum temperatures of ~15 °C (Chamley, 1997; Thiry, 2000). Illite and chlorite are less effected by pedogenesis (Wilson, 1999) and form by physical weathering of crystalline rocks (Chamley, 1989). Accordingly, a high amount of illite and chlorite in the sediments points to temperate to cool and less humid environments, with physical weathering as the dominant weathering type (Singer, 1984; Thiry, 2000). Weathering of volcanic rocks is an unlikely source for the GBA-core because the rare and thin tuffs that are recorded from the surroundings of the Vienna Basin (e.g., Rybár et al., 2019; Sant et al., 2020) would not suffice for the constant and high supply of smectite over the long time span documented from the core. We therefore assume that the smectite is mainly derived from regional soils. The ratio between smectite and kaolinite versus illite and chlorite is thus a proxy for the relation between chemical and physical weathering. The dominance of smectite and the relatively low contribution by kaolinite suggest a temperate climate with distinct seasonality (Singer, 1984). This clay-minerals-based interpretation is corroborated by palynological data by Kern et al. (2013), who analyzed a coeval, 6-m-long core from Hennersdorf, about 11 km south of the GBA-core (Fig. 1B). Kern et al. (2013) deduced a distinct seasonality in temperature with 24.7–27.9 °C during the warm season and 5.0–13.3 °C during the cold season. Mean annual precipitation was high, varying from 823 to 1529 mm but displayed a clear seasonality as well, with a wet season receiving 204–236 mm and a dry season ranging around 9–24 mm. Highest precipitation occurred during the warm season under a warm-temperate climate (Kern et al., 2013). A generally humid climate for the late Miocene was also described by Böhme et al. (2008). This climate state clearly explains the dominance of smectite over kaolinite.

The fairly constant clay mineral composition of the core interval from 80 to 35 m suggests rather stable climatic conditions during deposition of that interval. Starting from 35 m, however, a clear positive shift occurs in the illite/smectite and the chlorite/kaolinite ratios (Fig. 2F). We interpret the trend as a transition from a dominantly chemical weathering system to predominant physical weathering. Intuitively, one might explain this shift to drier conditions as resulting in stronger physical weathering (e.g., Gao et al., 2020). The positive shift in the illite/smectite and chlorite/kaolinite ratios, however, coincides with a decrease of the clay-silt/sand ratio due to increasing contributions of sand. Therefore, the increasing amounts of illite and chlorite are linked to increasing input of sand by fluvial transport. Consequently, we link the increased contribution by chlorite and illite to increased input from the hinterland as result of increased precipitation. This in turn dilutes the local, parautochthonous smectite record. The source of these clay minerals is the chlorite- and illite-rich Paleogene and Early Miocene paleosols of the Alpine catchment area (Kuhlemann et al., 2008). This increase of input from the hinterland is also expressed by the occurrence of reworked nannofossils, which are absent in the lower part of the core up to 44.8 m but become frequent thereafter.

4.3. Element distribution – primary signal and secondary dissolution

The sum of the most abundant elements (Ca, Fe, K, Ti, Mn) remains rather constant throughout the core, which is linked to the background sedimentation. The catchment area of the GBA-core was dominated by siliciclastic deposits of the RFU (Fig. 1). Thus, the baseline of the observed elemental contents is largely explained by their incorporation in the predominant phyllosilicates and feldspars derived from the RFU.

4.3.1. Shifts in input from the hinterland

Ti and Al are stable lithogenic elements, which are little effected by lake chemistry and postsedimentary and biologically processes (Koinig et al., 2003). These elements are generally interpreted as detrital inputs into the lake (Kylander et al., 2011; Boës et al., 2011; Davies et al., 2015). Due to their geochemical stability and unambiguous terrigenous origin, they are frequently used to normalize more mobile elements (Clift et al., 2008; Boës et al., 2011; Kylander et al., 2013; Matys Grygar et al., 2019).

The Zr/Ti ratio is a proxy for grain size, with lower values correlating with fine-grained sediment and higher values reflecting the contribution by coarse-grained particles because Zr tends to accumulate in coarser fractions (Dypvik and Harris, 2001; Kylander et al., 2011; Davies et al., 2015). In the GBA-core, Zr is significantly correlated with the occurrence of quartz (PCC = 0.86) and is bound to the coarse fraction of the sediment. The Zr/Ti ratio (Fig. 4) shows moderate fluctuations corresponding to the generally clay-rich composition of the sediment. An abrupt increase of the Zr/Ti ratio around 33 m is followed by a rapid decrease, which culminates in very low values around 25 m. Thus, that ratio documents a short shift in grain size due to increased fluvial input in the upper part of the core, followed by re-established calm offshore conditions with clay sedimentation. The correlation between K/Ti and Zr/Ti is generally good, but deviations occur in several intervals (e.g., 80–77 m, 71–68, 32–28 m) (note the inverted scale for K/Ti in Fig. 4). These phases of enhanced Zr/Ti and reduced K/Ti suggest increasing input of coarse sediment. The K/Ti ratio plots nearly constantly within the field expected for Al-silicates (relative to PAAS-values after Taylor and McLennan, 1985), except for samples 61.4–59.75 m, 56.0–55.8 m and around 32.5 m with enhanced K/Ti values. Of these, sample 32.5 m coincides with limestone gravel with low Ti content, thus differing distinctly from the surrounding Al-silicates. The other peaks, indicated is red squares in Fig. 4, are interpreted as analytical artifacts due to dilution effects by dominant phases such as high Fe (see Supplementary Fig. 1).

The K/Ti and Zr/Ti ratios both display considerable variation from 32.5 m onwards, which differs from the more stable patterns in the core-interval below.

The Mg/Al ratio (Fig. 5) is above the background Al-silicate level of 0.13 expected from PAAS values of Taylor and McLennan (1985). This suggests an additional Mg source, such as more Mg-rich Al-silicate minerals along with dolomite. Exceptions are the intervals around 24.8, 23.6 and 20.2 m in the uppermost core, with reduced input of dolomite. The Ca/Al record of the intervals 60.9–60.2 m, 49.3–43.3 m and 35.4–33.1 m plot close to the PAAS values of 0.18 (Fi. 5) and, therefore, Ca is bound here mainly to Al-silicates. This is supported by the bulk mineralogy, which failed to detect calcite in these samples. Consequently, positive excursions in the Ca/Al ratio are influenced by the input of calcite in carbonate. In sample 32.5 m, Ca and calcite are linked to input of fine carbonate gravel, as proven by sedimentological analysis. The Ca/Al and Mg/Al records are not correlated and the variability of the Mg/Al ratio ($\sigma = 0.02$) is much lower than that of the Ca/Al ratio ($\sigma = 0.17$, excluding sample 32.5 m). Therefore, dolomite and calcite had different sources with a comparatively more constant but smaller input of dolomite.

The Si/Al ratio (Fig. 6) of the GBA-core strongly overlaps with expected Si/Al values of Al-silicates based on PAAS data by Taylor and McLennan (1985). This indicates that most of the Si is represented by Al-silicates, which is unsurprising given that clay characterizes the core sediments. Samples plotting distinctly above this 'silicate-line' of 2.93% suggest an additional source for Si, which was identified mineralogically to be quartz. Thus, the Si/Al ratio indicates phases of increased quartz input (e.g., 43.3–27.6 m) alternating with phases of reduced input (e.g., 57.3–45.6 m). The Si/Al and Ti/Al records display rather stable values with moderate variability for the lower part of the core up to 32.5 m. An

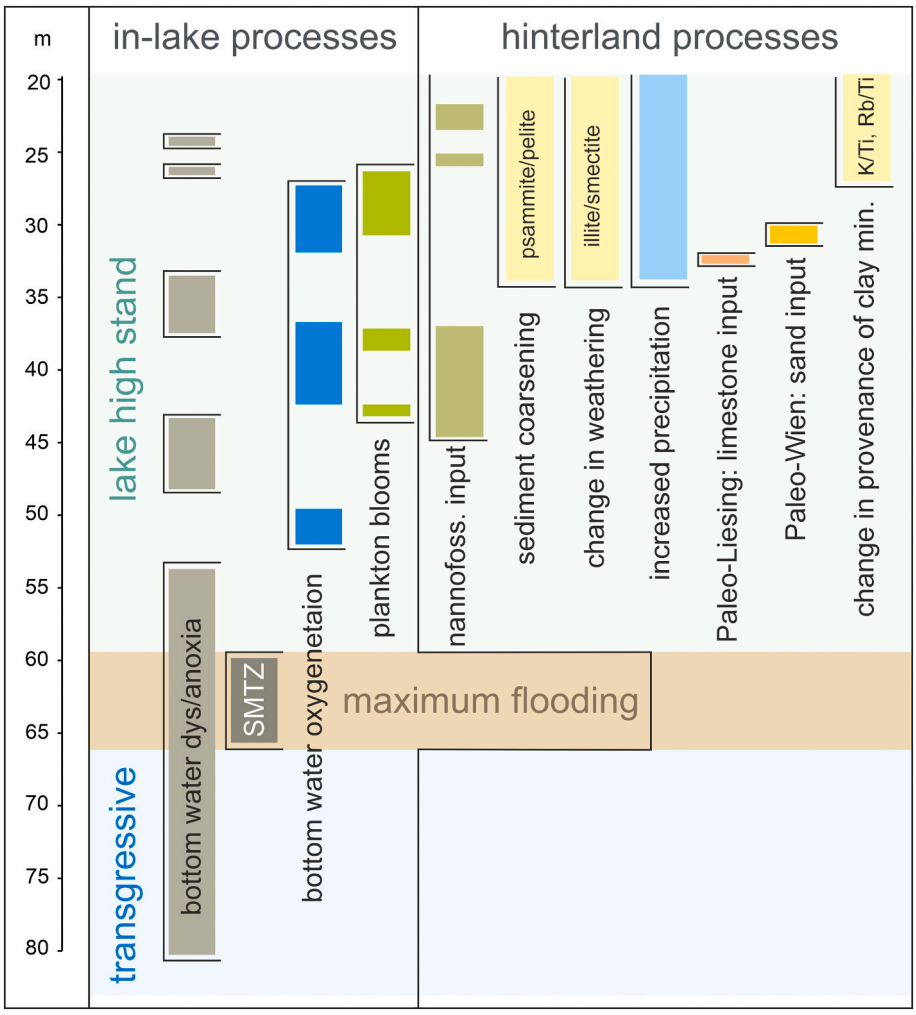

Fig. 9. Major environmental changes in the GBA-core as revealed by paleontological, mineralogical, sedimentological and geochemical proxies.

exception is a negative peak at 59.9 m, which reflects relative dilution due to high Fe values (Fig. 6). The input of sand at 31.4 m is reflected by a strong peak in both ratios. A shift towards lower values occurs in both ratios from 26.8 to 20.8 m. For the Ti/Al ratio this may indicate a change of clay mineral composition due to changes in provenance. The same mechanism may explain the reduced input of quartz as shown by the low Si/Al ratio.

4.3.2. In-lake processes

The Fe/Al ratio (Fig. 6) documents that most of the Fe is associated with clay minerals and is consistent with PAAS values of Taylor and McLennan (1985). A few samples, however, plot clearly above the expected Fe/Al values of 0.5 for Al-silicates (64.8, 59.9, 59.75, 57.3, 55.5, 47.4, 46.65, 38.6 m), suggesting an additional source for Fe. Similarly, the Ba/Al and Mn/Al ratios (Fig. 7) indicate that most of the Ba and Mn is associated with clay minerals except for the prominent peaks in samples 59.9 and 59.75 (a third peak in the Mn/Al ratio at 32.5 m is related to the presence of limestone gravel, which has much lower Al than the surrounding Al-silicates).

Paleontological data, such as the lack of molluscs and ostracods and the high amount of plant debris, suggest originally dysoxic or anoxic conditions during the formation of the sample intervals with the marked Fe, Mn and Ba accumulations. In such environments, Fe concentrations are frequently caused by authigenic formation of greigite and/or pyrite due to sulfate reduction by anaerobic sulfur bacteria and by magnetotactic sulfur bacteria along sulfate-methane transition zones (SMTZ) (Watanabe et al., 2004; Demory et al., 2005; Vasiliev et al., 2008). Sulfide-formation-driven Fe accumulations in Holocene deposits of the Black Sea were explained by Lyons and Severmann (2006) and Dekov et al. (2020) by the so-called "benthic Fe redox shuttle". In this scenario, Fe-oxides are dissolved under suboxic conditions on the shelf and the produced Fe^{2+} becomes mobilized. It then becomes transported to deeper euxinic parts of the basin where it reacts with H_2S to form iron sulfides. Given that Lake Pannon was a huge euxinic basin with polyhaline salinity, the presence of mechanisms known from Black Sea environments would be consistent. Thus, the Fe/Al-peaks might correspond to the formation of iron sulfides in former sulfate-methane transition zones (SMTZ) as also described by Harzhauser et al. (2018) from Lake Pannon deposits of the Vienna Basin. Similarly, Ba2+ is released to the pore water in anoxic sediments in which sulfate reduction dominates (Liguori et al., 2016). The released Ba will diffuse upward and will precipitate as barium sulfate above the SMTZ, forming a Barium front (Dickens, 2001). Alternatively, it will be associated with Fe—Mn oxides (Carter et al., 2020). This process typically occurs closely above the SMTZ, and barium fronts in sediments are often interpreted as former SMTZs (Torres et al., 1996; Dickens, 2001; Riedinger et al., 2006). Mn-enrichment in marine and lacustrine sediments is explained by diffusion of reduced Mn^{2+} from deeper, anoxic sediments into the overlying water, where Mn becomes trapped in oxides at the sediment surface at the presence of slightly oxic bottom waters (Reitz et al., 2006). Especially in mesotrophic, deep lakes with anoxic sediment overlain by an oxic water-column, Mn will concentrate at the sediment surface by

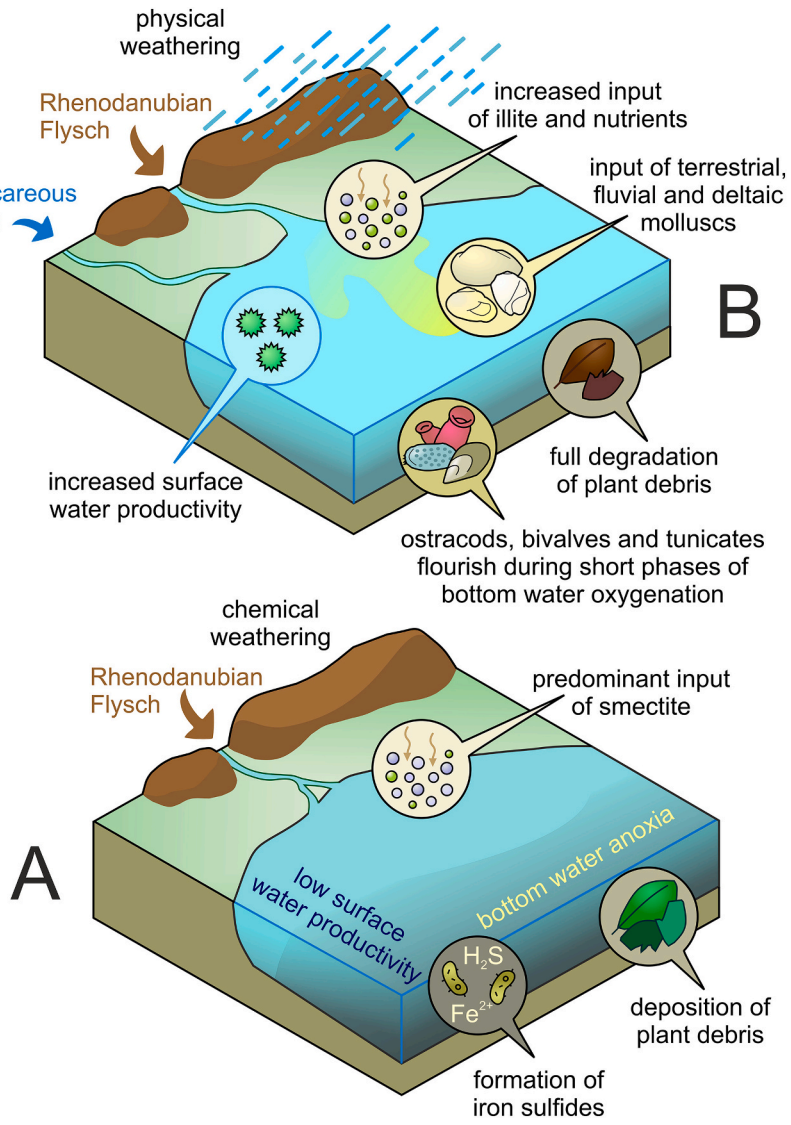

Fig. 10. Idealized paleoenvironmental reconstructions of Lake Pannon along the western margin of the Vienna Basin. ***A.*** *maximum* extent of Lake Pannon, with widespread bottom-water anoxia, reduced terrestrial input and low surface productivity (based on lower part of the GBA-core, 80–44.8 m). **B.** Early highstand of Lake Pannon; increased nutrient input causes nannoplankton blooms. Short phases of lake bottom oxidation stimulate settlement by benthic organisms (based on upper part of the GBA-core, 44.8–20 m).

geochemical focusing (Schaller and Wehrli, 1997; Naeher et al., 2013). Such buried zones of Fe and Mn enrichments correspond to phases of low sedimentation (Granina et al., 2003).

Thus, the tight correlation of Fe, Ba and Mn during the peaks around 60 m results from closely related biogeochemical processes that occur at the anoxic/oxic interface, leading to enrichment of these elements at the sediment surface under low sedimentation. Within the GBA-core we interpret this phase as the maximum flooding of Lake Pannon when input from the hinterland was minimal and anoxic conditions of a SMTZ became established in the sediment.

This interpretation seemingly contradicts the S/Al and S/Ti ratios, which display two intervals at 64.8–56.2 m and 41.8–33.8 with very low values due to the near absence of S (Fig. 8). The upper low-S interval coincides with the presence of rich benthic faunas, documenting originally oxidized bottom conditions. The lower low-S interval, however, covers the samples, which are interpreted above as indicative for dysoxic or anoxic environments. An explanation for this apparent deviation would be that, during subsequent oxidation of the pyrite, Fe-oxides and sulphate formed. The latter is likely to have diffused out of the zone of formation or was removed by groundwater. The iron oxides remained as limonite and goethite (Rösler, 1987). We do not know when this pyrite oxidation occurred.

The presence of siderite in samples 59.75 and 59.9 is also evidence for an anoxic depositional environment. This ferrous carbonate needs oxygen-free environments and high alkalinity in the form of high DIC (Lin et al., 2019; Koo and Kim, 2020). It precipitates as one of the earliest minerals in the sediment by bacterial methanogenesis (Curtis et al., 1986; Hałas and Chlebowski, 2004), but will not form in presence of hydrogen sulfide because this would lead to iron sulfide formation (Lin et al., 2019). Thus, this short interval around 60 m indicates anoxic conditions and high organic matter degradation rates.

5. Conclusions

The GBA-core covers a timespan when Lake Pannon was fully established and covered the entire Pannonian basins system (Magyar, 2021). At that time the global Tortonian Thermal Maximum was in full swing (Westerhold et al., 2020) and precipitation increased distinctly (Böhme et al., 2008), providing an ample supply of water for a rise of the lake level. So far, however, no geological record has described the environmental feed-backs during this last Miocene thermal optimum in detail. Our proxy data document a cascade of environmental shifts within the lake and in the hinterland (Fig. 9). The lower part of the core captures the terminal transgressive phase and the maximum extend of Lake Pannon, when hostile environments became established on the lake bottom. No benthic organisms could settle offshore environments, and

plant debris became incorporated in the sediment (Fig. 10A). Iron sulfide formation was common during this phase, but the original pyrite is now largely degraded into iron oxides, which led to a loss of S.

The maximum flooding of the lake is indicated in the GBA-core around 60 m by marked peaks in Fe, Ba and Mn, which point to the establishment of several SMTZs (Fig. 9). The Zr/Ti, K/Ti and Rb/Ti ratios document that this phase coincided with strongly reduced input of coarse sediment and deposition of fine clay, which would be expected during a maximum flooding. Siderite points to the originally anoxic conditions and formed during a short interval in which no hydrogen sulfide was present. Surface water productivity was low and no nannoplankton blooms occurred during this phase. The sediment and clay mineralogy document stable and calm conditions with reduced terrigenous input and predominantly chemical weathering in the hinterland (Fig. 10A).

During the transition into the lake highstand, short phases of bottom-water oxidation enabled the development of a few, short-lived bivalve pavements around 50.2 to 50.5 m and are reflected by rare bioturbation. The input from the hinterland, however, did not change and there are no signs for elevated surface water productivity. Starting around 45 m, reworked Cretaceous nannoplankton indicates increased input of nannofossils from the RFU (Fig. 9). The coincident increased input of nutrients triggered blooms of autochthonous nannoplankton (Fig. 10B). Starting from about 35 m, the change in the clay-silt/sand ratio and the shift in the illite/smectite ratio indicate a coarsening of the sediment and a change of the prevailing weathering regime, which is most likely related to increased precipitation. Physical weathering increased and stronger precipitation mobilized detritic kaolinite from the hinterland. The positive illite/smectite trend continued throughout the upper core, whereas the fluvial influx ceased rapidly and clay sedimentation prevailed again. Therefore, the shift in clay mineral composition is not explained by the single fluvial event but reflects a constant climatic signal. The coincident negative shift in the K/Ti ratio might indicate an increased contribution of chemically leached material from the hinterland, which became mobilized by stronger precipitation. Input of fine limestone gravel at 32.5 m indicates a short-lived source from the Calcareous Alps, which might be represented by the Paleo-Liesing river (Fig. 1C). At 30.7 m, enhanced input of coarser siliciclastics set in, which were derived again from the RFU. Deltaic, riverine, and terrestrial molluscs were washed into the lake, most probably by the Paleo-Wien river. This fluvial episode ceased soon, and offshore conditions were re-established at 30.15 m. Subsequently, a rapid alternation of oxic and dysoxic conditions characterized the lake bottom up to the top of the core (Fig. 9). Shifts in the Ti/Al, Ti/Al and Si/Al ratios, which are all based on terrigenous elements, hint at a change of provenance of clay minerals in the upper part of the core above 27.6 m.

The prevailing dysoxic bottom conditions became frequently replaced in the upper part of the core by fully oxygenated environments, which stimulated settlement by benthos such as bivalves, ostracods and tunicates, and caused full degradation of plant debris. The presence of stenohaline tunicates indicates that the increased precipitation did not cause a decrease in salinity, at least in deeper offshore environments. Based on the ecological requirements of modern tunicates, we assume a polyhaline water salinity of about 20 psu for this phase of Lake Pannon around 10.4 Ma. This is substantially higher than the 15 psu discussed in the literature thus far, and forms an intriguing topic for future studies.

Supplementary data to this article can be found online at https://doi.org/10.1016/j.palaeo.2022.111332.

Declaration of Competing Interest

None.

Data availability

all data are in the supplementary file

Acknowledgements

We thank Vera Hammer (NHMW) for X-ray Diffraction analysis. This project was financed by the Geological Survey Vienna (Austria). We thank two anonymous reviewers for their constructive comments and Howard Falcon-Lang (Royal Holloway University of London) for his careful editorial work.

References

Auer, G., Piller, W.E., Harzhauser, M., 2015. Two distinct decadal and centennial cyclicities forced marine upwelling intensity and precipitation during the late early Miocene in Central Europe. Clim. Past 11, 283–303. https://doi.org/10.5194/cp-11-283-2015.

Boës, X., Rydberg, J., Martinez-Cortzas, A., Bindler, R., Renberg, I., 2011. Evaluation of conservative lithogenic elements (Ti, Zr, Al, and Rb) to study anthropogenic element enrichments in lake sediments. J. Paleolimnol. 46, 75–87. https://doi.org/10.1007/s10933-011-9515-z.

Böhme, M., Ilg, A., Winklhofer, M., 2008. Late Miocene "washhouse" climate in Europe. Earth Planet. Sci. Lett. 275, 393–401. https://doi.org/10.1016/j.epsl.2008.09.011.

Borzi, A., Harzhauser, M., Piller, W.E., Strauss, P., Siedl, W., Dellmour, R., 2022. Late Miocene Evolution of the Paleo-Danube Delta (Vienna Basin, Austria). Glob. Planet. Chang. 103769 https://doi.org/10.1016/j.gloplacha.2022.103769.

Botka, D., Magyar, I., Csoma, V., Tóth, E., Šujan, M., Ruszkiczay-Rüdiger, Z., Chyba, A., Braucher, R., Sant, K., Ćorić, S., Baranyi, V., Bakrač, K., Krizmanić, K., Bartha, I.R., Szabó, M., Silye, L., 2019. Integrated stratigraphy of the Guşterița clay pit: a key section for the early Pannonian (late Miocene) of the Transylvanian Basin (Romania). Aust. J. Earth Sci. 112, 221–247. https://doi.org/10.17738/ajes.2019.0013.

Carter, S.C., Paytan, A., Griffith, E.M., 2020. Toward an improved understanding of the marine Barium Cycle and the application of marine barite as a paleoproductivity proxy. Minerals 10, 421. https://doi.org/10.3390/min10050421.

Chamley, H., 1997. Clay mineral sedimentation in the ocean. In: Paquet, H., Clauer, N. (Eds.), Soils and Sediments. Mineralogy and Geochemistry. Springer, Berlin, pp. 269–302.

Chamley, H., 1989. In: Clay Sedimentology. Springer-Verlag, Berlin, Heidelberg, New York, p. 623.

Clift, P.D., Hodges, K.V., Heslop, D., Hannigan, R., Van Long, H., Calves, G., 2008. Correlation of Himalayan exhumation rates and asian monsoon intensity. Nat. Geosci. 1, 875–880. https://doi.org/10.1038/ngeo351.

Ćorić, S., 2021. Calcareous nannofossils from the middle/upper Miocene succession of Pécs-Danitzpuszta, southern Hungary: cosmopolitan Paratethys and endemic Lake Pannon assemblages. Földtani Közlöny 151, 253–266. https://doi.org/10.23928/foldt.kozl.2021.151.3.25.

Ćorić, S., Hohenegger, J., 2008. Quantitative analyses of calcareous nannoplankton assemblages from the Baden-Sooss section (Middle Miocene of Vienna Basin, Austria). Geol. Carpath. 59, 447–460.

Ćorić, S., Kovačić, M., Bortek, Ž., Marković, F., Vrsaljko, D., 2017. Changes in Middle/Upper Miocene calcareous nannoplankton assemblages (Central Paratethys; Našice; Croatia) – paleoecology and stratigraphy. In: 7th International Workshop Neogene of Central and South-Eastern Europe, 28–31.5. Abstracts Book, Velika.

Curtis, C.D., Coleman, M.L., Love, L.G., 1986. Pore water evolution during sediment burial from isotopic and mineral chemistry of calcite, dolomite and siderite concretions. Geochim. Cosmochim. Acta 50, 2321–2334. https://doi.org/10.1016/0016-7037(86)90085-2.

Cziczer, I., Magyar, I., Pipík, R., Böhme, M., Ćorić, S., Bakrač, K., Sütö-Szentai, M., Lantos, M., Babinszki, E., Müller, P., 2009. Life in the sublittoral zone of long-lived Lake Pannon: paleontological analysis of the Upper Miocene Szák Formation, Hungary. Int. J. Earth Sci. 98, 1741–1766. https://doi.org/10.1007/s00531-008-0322-3.

Davies, S.J., Lamb, H., Roberts, S.J., 2015. Micro-XRF core scanning in palaeolimnology: recent developments. In: Croudace, I.W., Rothwell, R.G. (Eds.), Micro-XRF Studies of Sediment Cores: Applications of a Non-destructive Tool for the Environmental Sciences. Developments in Paleoenvironmental Research, 17, pp. 189–226. https://doi.org/10.1007/978-94-017-9849-5_7.

Dekov, V.M., Darakchieva, V.Y., Billström, K.M., Garbe-Schönberg, C.D., Kamenov, G.D., Gallinari, M., Dimitrov, L., Ragueneau, O., Kooijman, E., 2020. Element enrichment and provenance of the detrital component in Holocene sediments from the western Black Sea. Oceanologia 62, 139–163. https://doi.org/10.1016/j.oceano.2019.10.001.

Demory, F., Oberhänsli, H., Nowaczyk, N., Gottschalk, M., Wirth, R., Naumann, R., 2005. Detrital input and early diagenesis in sediments from Lake Baikal revealed by rock magnetism. Glob. Planet. Chang. 46, 145–166. https://doi.org/10.1016/j.gloplacha.2004.11.010.

Dickens, G.R., 2001. Sulfate profiles and barium fronts in sediment on the Blake Ridge: present and past methane fluxes through a large gas hydrate reservoir. Geochim. Cosmochim. Acta 65, 529–543. https://doi.org/10.1016/S0016-7037(00)00556-1.

Duverger, A., Berg, J.S., Busigny, V., Guyot, F., Bernard, S., Miot, J., 2020. Mechanisms of Pyrite formation promoted by sulfate-reducing bacteria in pure culture. Front. Earth Sci. 8, 588310 https://doi.org/10.3389/feart.2020.588310.

Dypvik, H., Harris, N.B., 2001. Geochemical facies analysis of finegrained siliciclastics using Th/U, Zr/Rb and (Zr/Rb)/Sr ratios. Chem. Geol. 181, 131–146. https://doi.org/10.1016/S0009-2541(01)00278-9.

Füchtbauer, H., 1959. Zur Nomenklatur der Sedimentgesteine. Erdöl Kohle 12, 605–613.
Gao, Y., Gao, Y., Ibarra, D.E., Du, X., Dong, T., Liu, Z., Wang, C., 2020. Clay mineralogical evidence for mid-latitude terrestrial climate change from the latest Cretaceous through the earliest Paleogene in the Songliao Basin, NE China. https://doi.org/10.5194/cp-2020-36. Climate of the Past Discussions, preprint.
Granina, L., Müller, B., Wehrli, B., 2003. Origin and dynamics of Fe and Mn sedimentary layers in Lake Baikal. Chem. Geol. 205, 55–72. https://doi.org/10.1016/j.chemgeo.2003.12.018.
Gross, M., Piller, W.E., Scholger, R., Gitter, F., 2011. Biotic and abiotic response to palaeoenvironmental changes at Lake Pannons'western margin (Central Europe, late Miocene). Palaeogeogr. Palaeoclimatol. Palaeoecol. 312, 181–193. https://doi.org/10.1016/j.palaeo.2011.10.010.
Grupe, S., Payer, T., Pfleiderer, S., 2021. Donauterrassen und Donaukiese im Bereich des Wiener Stadtgebietes. In: Jahrbuch der Geologischen Bundesanstalt, 161, pp. 29–38. https://opac.geologie.ac.at/ais312/dokumente/JB1611_029_A_Grupe_etal.pdf.
Hałas, S., Chlebowski, R., 2004. Unique siderite occurrence in Baltic Sea: a clue to siderite-water oxygen isotopefractionation at low temperatures. Geol. Q. 48, 317–322. https://gq.pgi.gov.pl/article/view/7355.
Hammer, Ø., 2021. PAleontological Statistics Version 4.06. Reference Manual, 290 pp. Natural History Museum. University of Oslo, Oslo. https://www.nhm.uio.no/english/research/infrastructure/past/downloads/past4manual.pdf.
Hammer, Ø., Harper, D.A.T., Ryan, P.D., 2001. PAST: paleontological statistics software package for education and data analysis. Palaeontol. Electron. 4 (1), 1–9.
Harzhauser, M., Mandic, O., 2004. The muddy bottom of Lake Pannon - a challenge for dreissenid settlement (Late Miocene; Bivalvia). Palaeogeogr. Palaeoclimatol. Palaeoecol. 204, 331–352. https://doi.org/10.1016/S0031-0182(03)00735-1.
Harzhauser, M., Mandic, O., 2008. Neogene lake systems of Central and South-Eastern Europe: Faunal diversity, gradients and interrelations. Palaeogeogr. Palaeoclimatol. Palaeoecol. 260, 417–434. https://doi.org/10.1016/j.palaeo.2007.12.013.
Harzhauser, M., Daxner-Höck, G., Piller, W.E., 2004. An integrated stratigraphy of the Pannonian (Late Miocene) in the Vienna Basin. Aust. J. Earth Sci. 95 (96), 6–19.
Harzhauser, M., Latal, C., Piller, W.E., 2007a. The stable isotope archive of Lake Pannon as a mirror of late Miocene climate change. Palaeogeogr. Palaeoclimatol. Palaeoecol. 249, 335–350. https://doi.org/10.1016/j.palaeo.2007.02.006.
Harzhauser, M., Piller, W.E., Latal, C., 2007b. Geodynamic impact on the stable isotope signatures in a shallow epicontinental sea. Terra Nova 19, 1–7. https://doi.org/10.1111/j.1365-3121.2007.00755.x.
Harzhauser, M., Kranner, M., Mandic, O., Ćorić, S., Siedl, W., 2022. High resolution late Miocene sediment accommodation rates and subsidence history in the austrian part of the Vienna Basin. Mar. Pet. Geol. https://doi.org/10.1016/j.marpetgeo.2022.105872.
Harzhauser, M., Kern, A., Soliman, A., Minati, K., Piller, W.E., Danielopol, D., Zuschin, M., 2008. Centennial- to decadal-scale environmental shifts in and around Lake Pannon (Vienna Basin) related to a major late Miocene lake-level rise. Palaeogeogr. Palaeoclimatol. Palaeoecol. 270, 102–115. https://doi.org/10.1016/j.palaeo.2008.09.00.
Harzhauser, M., Mandic, O., Kern, A.K., Piller, W.E., Neubauer, T.A., Albrecht, C., Wilke, T., 2013. Explosive demographic expansion by dreissenid bivalves as a possible result of astronomical forcing. Biogeosciences 10, 8423–8431. https://doi.org/10.5194/bg-10-8423-2013.
Harzhauser, M., Mandic, O., Kranner, M., Lukeneder, P., Kern, A.K., Gross, M., Carnevale, G., Jawecki, C., 2018. The Sarmatian/Pannonian boundary at the western margin of the Vienna Basin (City of Vienna, Austria). Aust. J. Earth Sci. 111, 26–47. https://doi.org/10.17738/ajes.2018.0003.
Hernes, P.J., Miller, R.L., Dyda, R.Y., Bergamachi, B.A., 2020. Vegetation vs. anoxic controls on degradation of plant litter in a restored wetland. Front. Environ. Sci. 8, 564603.
Kern, A.K., Harzhauser, M., Piller, W.E., Mandic, O., Soliman, A., 2012. Strong evidence for the influence of solar cycles on a late Miocene lake system revealed by biotic and abiotic proxies. Palaeogeogr. Palaeoclimatol. Palaeoecol. 329–330, 124–136. https://doi.org/10.1016/j.palaeo.2012.02.023.
Kern, A.K., Harzhauser, M., Soliman, A., Piller, W.E., Mandic, O., 2013. High-resolution analysis of Upper Miocene lake deposits: evidence for the influence of Gleissberg-band solar forcing. Palaeogeogr. Palaeoclimatol. Palaeoecol. 370, 176–183. https://doi.org/10.1016/j.palaeo.2012.12.005.
Koinig, K.A., Shotyk, W., Lotter, A.F., Ohlendorf, C., Sturm, M., 2003. 9000 years of geochemical evolution of lithogenic major and trace elements in the sediment of an alpine lake – the role of climate, vegetation, and land-use history. J. Paleolimnol. 30, 307–320. https://doi.org/10.1023/A:1026080712312.
Koo, T., Kim, J., 2020. Controls on the Formation and Stability of Siderite(FeCO3) and Chukanovite (Fe(CO3) (OH)2)in reducing Environment. Minerals 10, 156. https://doi.org/10.3390/min10020156.
Kováč, M., Baráth, I., Kováčová-Slamková, M., Pipík, R., Hlavatý, I., Hudáčková, N., 1998. Late Miocene paleoenvironments and sequence stratigraphy: Northern Vienna Basin. Geol. Carpath. 49 (6), 445–458.
Kováč, M., Márton, E., Oszczypko, N., Vojtko, R., Hók, J., Králiková, S., Plašienka, D., Klučiar, T., Hudáčková, N., Oszczypko-Clowes, M., 2017. Neogene palaeogeography and basin evolution of the Western Carpathians, Northern Pannonian domain and adjoining areas. Glob. Planet. Chang. 155, 133–154. https://doi.org/10.1016/j.gloplacha.2017.07.004.
Kuhlemann, J., Taubald, H., Vennemann, T., Dunkl, I., Frisch, W., 2008. Clay mineral and geochemical composition of Cenozoic paleosol in the Eastern Alps (Austria). Aust. J. Earth Sci. 101, 60–69.
Küpper, F., 1965. Geologie von Wien. Kurzfassung 1964. 194 pp. Hollinek, Borntraeger, Wien-Berlin. https://opac.geologie.ac.at/ais312/dokumente/K%C3%BCpper_Geologie_Wien_1965.pdf.
Kylander, M.E., Ampel, L., Wohlfarth, B., Veres, D., 2011. High-resolution X-ray fluorescence core scanning analysis of Les Echets (France) sedimentary sequence: new insights from chemical proxies. J. Quat. Sci. 26, 109–117. https://doi.org/10.1002/jqs.1438.
Kylander, M.E., Klaminder, J., Wohlfarth, B., Löwenmark, L., 2013. Geochemical responses to paleoclimatic changes in southern Sweden since the late glacial: the Hässeldala Port lake sediment record. J. Paleolimnol. 50, 57–70. https://doi.org/10.1007/s10933-013-9704-z.
Lambert, G., 2005. Ecology and natural history of the protochordates. Can. J. Zool. 83, 34–50. https://doi.org/10.1139/z04-156.
Liguori, B.T.P., Gomes de Almeida, M., Rezende, C.E., 2016. Barium and its importance as an indicator of (Paleo)Productivity. In: Anais da Academia Brasileira de Ciências, 88, pp. 2093–2103.
Lin, C.Y., Turchyn, A.V., Krylov, A., Antler, G., 2019. The microbially driven formation of siderite in salt marsh sediments. Geobiology 18, 207–224. https://doi.org/10.1111/gbi.12371.
Lirer, F., Harzhauser, M., Pelosi, N., Piller, W.E., Schmid, H.P., Sprovieri, M., 2009. Astronomically forced teleconnection between Paratethyan and Mediterranean sediments during the Middle and late Miocene. Palaeogeogr. Palaeoclimatol. Palaeoecol. 275, 1–13. https://doi.org/10.1016/j.palaeo.2009.01.006.
Locatelli, E., 2014. The exceptional preservation of plant fossils: a review of taphonomic pathways and biases in the fossil record. Paleontol. Soc. Pap. 20, 237–258. https://doi.org/10.1017/S1089332600002874.
Lyons, T.W., Severmann, S., 2006. A critical look at iron paleoredox proxies: New insights from modern euxinic marine basins. Geochim. Cosmochim. Acta 70, 5698–5722. https://doi.org/10.1016/j.gca.2006.08.021.
Magyar, I., 1995. Late Miocene mollusc biostratigraphy in the eastern part of the Pannonian Basin (Tiszántúl, Hungary). Geol. Carpath. 46, 29–36.
Magyar, I., 2021. Chronostratigraphy of clinothem-filled non-marine basins: dating the Pannonian Stage. Glob. Planet. Chang. 205, 103609 https://doi.org/10.1016/j.gloplacha.2021.103609.
Magyar, I., Geary, D.H., Müller, P., 1999. Paleogeographic evolution of the late Miocene Lake Pannon in Central Europe. Palaeogeogr. Palaeoclimatol. Paleoecol. 147, 151–167. https://doi.org/10.1016/S0031-0182(98)00155-2.
Magyar, I., Radivojević, D., Sztanó, O., Synak, R., Ujszászi, K., Pócsik, M., 2013. Progradation of the paleo-Danube shelf margin across the Pannonian Basin during the late Miocene and early Pliocene. Glob. Planet. Chang. 103, 168–173. https://doi.org/10.1016/j.gloplacha.2012.06.007.
Marunteanu, M., 1997. Evolution line of the endemic genus Noelaerhabdus Pannonian; Pannonian Basin. Acta Palaeontol. Roman. 1, 96–100.
Matys Grygar, T., Mach, K., Martínez, M., 2019. Checklist for the use of potassium concentrationsin siliciclastic sediments as paleoenvironmental archives. Sediment. Geol. 382, 75–84. https://doi.org/10.1016/j.sedgeo.2019.01.010.
Moore, D.M., Reynolds Jr., R.C., 1989. In: X-Ray Diffraction and their Identification and Analysis of Clay Minerals. Oxford University Press, Oxford, p. 332 pp..
Naeher, S., Gilli, A., North, R.P., Hamann, Y., Schubert, C.J., 2013. Tracing bottom water oxygenation with sedimentary Mn/Fe ratios in Lake Zurich, Switzerland. Chem. Geol. 352, 125–133. https://doi.org/10.1016/j.chemgeo.2013.06.006.
Neubauer, T.A., Harzhauser, M., Kroh, A., 2013. Phenotypic evolution in a fossil gastropod species lineage: evidence for adaptive radiation? Palaeogeogr. Palaeoclimatol. Palaeoecol. 370, 117–126. https://doi.org/10.1016/j.palaeo.2012.11.025.
Neubauer, T.A., Georgopoulou, E., Harzhauser, M., Mandic, O., Kroh, A., 2016a. Predictors of shell size in long-lived lake gastropods. J. Biogeogr. 43, 2062–2074. https://doi.org/10.1111/jbi.12777.
Neubauer, T.A., Harzhauser, M., Mandic, O., Kroh, A., Georgopoulou, E., 2016. Evolution, turnovers and spatial variation of the gastropod fauna of the late Miocene biodiversity hotspot Lake Pannon. Palaeogeogr. Palaeoclimatol. Palaeoecol. 442, 84–95. https://doi.org/10.1016/j.palaeo.2015.11.016.
Österreichisches Normungsinstitut, 1988. Physikalische Bodenuntersuchungen-Bestimmung des Wassergehaltes und des Wasseranteils. In: ÖNORM L1062. Austrian Standards Plus GmbH, Wien, p. 2.
Papp, A., 1951. Das Pannon des Wiener Beckens. In: Mitteilungen der Geologischen Gesellschaft in Wien.
Peleo-Alampay, A.M., Mead, G.A., Wei, W., 1999. Unusual Oligocene Braarudosphaera-rich layers of the South Atlantic and their paleoceanographic implications. J. Nannoplankton Res. 21, 17–26.
Pool, T.K., Luis, S., Olden, J.D., 2013. Assessing Lethal Dissolved Oxygen Tolerance for Invasive Tunicate Ciona savignyi in Puget Sound. Northwest Sci. 87, 106–113. https://doi.org/10.3955/046.087.0203.
Reitner, H., Malecki, G., Roetzel, R., 2005. SedPakWin – SedPacMac – Characterization of Sediments by Grainsize Analysis. Geophysical Research Abstracts, 7, EGU General assembly Vienna, 24.-29. April 2005, Sref-ID: 1607-7962/gra/EGU05-A-04297.
Reitz, A., Thomson, J., de Lange, G.J., Hensen, C., 2006. Source and development of large manganese enrichments above eastern Mediterranean sapropel S1. Paleoceanogr. Paleoclimatol. 21, PA3007. https://doi.org/10.1029/2005PA001169.
Riedinger, N., Kasten, S., Gröger, J., Franke, C., Pfeifer, K., 2006. Active and buried authigenic barite fronts in sediments from the Eastern Cape Basin. Earth Planet. Sci. Lett. 241, 876–887. https://doi.org/10.1016/j.epsl.2005.10.032.
Rösler, H.J., 1987. Lehrbuch der Mineralogie. 4. durchgesehene und erweiterte Auflage. Deutscher Verlag für Grundstoffindustrie (VEB), Leipzig, 384 pp., ISBN 3-342-00288-3.
Rybár, S., Šarinová, K., Sant, K., Kuiper, K.F., Kováčová, M., Vojtko, R., Reiser, M.K., Fordinál, K., Teodoridis, V., Nováková, P., Vlček, T., 2019. New 40Ar/39Ar, fission track and sedimentological data on a middle Miocene tuff occurring in the Vienna

Basin: implications for the north-western Central Paratethys region. Geol. Carpath. 70, 386–404. https://doi.org/10.2478/geoca-2019-0022.
Sant, K., Kuiper, K.F., Rybár, S., Grunert, P., Harzhauser, M., Mandic, O., Jamrich, M., Šarinová, K., Hudáčková, N., Krijgsman, W., 2020. 40Ar/39Ar geochronology using high sensitivity mass spectrometry: examples from middle Miocene horizons of the Central Paratethys. Geol. Carpath. 71, 166–182. https://doi.org/10.31577/GeolCarp.71.2.5.
Schaller, T., Wehrli, B., 1997. Geochemical focusing of manganese in lake sediments - an indicator of deep-water oxygen. Aquat. Geochem. 2, 359–378. https://doi.org/10.1007/BF00115977.
Schramm, R., 2012. Röntgenfluoreszenzanalyse in der Praxis. Fluxana, Bedburg-Hau, 1. Auflage, 98 pp.
Schroll, E., 1974. Analytische Geochemie. Band 1 Methodik. Ferdinand Enke Verlag, Stuttgart, 292 pp.
Schütz, K., Harzhauser, M., Rögl, F., Ćorić, S., Galovic, I., 2007. Foraminiferen und Phytoplankton aus dem unteren Sarmatium des südlichen Wiener Beckens (Petronell, Niederösterreich). In: Jahrbuch der Geologischen Bundesanstalt, 147, pp. 449–488. https://www.zobodat.at/pdf/JbGeolReichsanst_147_0449-0488.pdf.
Shenkar, N., Swalla, B.J., 2022. Global diversity of Ascidiacea. Plos One 6 (6). https://doi.org/10.1371/journal.pone.0020657 e20657.
Singer, A., 1984. The paleoclimatic interpretation of clay minerals in sediments — a review. Earth Sci. Rev. 21, 251–293. https://doi.org/10.1016/0012-8252(84)90055-2.
Sztanó, O., Sebe, K., Csillag, G., Magyar, I., 2015. Turbidites as indicators of paleotopography, late Miocene Lake Pannon, Western Mecsek, Hungary. Geol. Carpath. 66, 331–344. https://doi.org/10.1515/geoca-2015-0029.
Taut, T., Kleeberg, R., Bergmann, J., 1998. The new Seifert Rietveld program BGMN and its application to quantitative phase analysis. Mater. Sci. (Bull. Czech Slovak Crystallogr. Assoc.) 5, 55–64. http://www.xray.cz/ms/bul98-1/bul-taut.pdf.
Taylor, S.R., McLennan, S.M., 1985. The Continental Crust its composition and cvolution. xvi + 312 pp. Blackwell Scientific., Oxford, London, Edinburgh, Boston, Palo Alto, Melbourne.
Thiel, J., Byrne, J.M., Kappler, A., Schink, B., Pester, M., 2019. Pyrite formation from FeS and H2S is mediated through microbial redox activity. PNAS 116, 6897–6902. https://doi.org/10.1073/pnas.1814412116.
Thiry, M., 2000. Paleoclimatic interpretation of clay minerals in marine deposits: an outlook from the continental origin. Earth Sci. Rev. 49, 201–221. https://doi.org/10.1016/S0012-8252(99)00054-9.
Torres, M.E., Brumsack, H.J., Bohrmann, G., Emeis, K.C., 1996. Barite fronts in continental margin sediments: a new look at barium remobilization in the zone of sulfate reduction and formation of heavy barites in diagenetic fronts. Chem. Geol. 127, 125–139. https://doi.org/10.1016/0009-2541(95)00090-9.
Varol, O., Houghton, S., 1996. A review and classification of fossil didemnid ascidian spicules. J. Micropalaeontol. 15, 135–149.
Vasiliev, I., Franke, C., Meeldijk, J.D., Dekkers, M.J., Langereis, C.G., Krijgsman, W., 2008. Putative greigite magnetofossils from the Pliocene epoch. Nat. Geosci. 1, 782–786. https://doi.org/10.1038/ngeo335.
Vázquez, E., Young, C.M., 1996. Responses of compound ascidian larvae to haloclines. Mar. Ecol. Prog. Ser. 133, 179–190. https://www.jstor.org/stable/24856117.
Vázquez, E., Young, C.M., 2000. Effects of low salinity on metamorphosis in estuarine colonial ascidians. Invertebr. Biol. 119, 433–444. https://doi.org/10.1111/j.1744-7410.2000.tb00113.x.
Watanabe, T., Naraoka, H., Nishimura, M., Kawai, T., 2004. Biological and environmental changes in Lake Baikal during the late Quaternary inferred from carbon, nitrogen and sulfur isotopes. Earth Planet. Sci. Lett. 222, 285–299. https://doi.org/10.1016/j.epsl.2004.02.009.
Wessely, G., 2006. Niederösterreich. In: Geologie der Österreichischen Bundesländer. Geologische Bundesanstalt Wien, 416 pp.
Westerhold, T., Marwan, N., Drury, A.J., Liebrand, D., Agnini, C., Anagnostou, E., Barnet, J.S.K., Bohaty, S.M., De Vleeschouwer, D., Florindo, F., Frederichs, T., Hodell, D.A., Holbourn, A.E., Kroon, D., Lauretano, V., Littler, K., Lourens, L.J., Lyle, M., Pälike, H., Röhl, U., Tian, J., Wilkens, R.H., Wilson, P.A., Zachos, J.C., 2020. An astronomically dated record of Earth's climate and its predictability over the last 66 million years. Science 369 (6509), 1383–1387. https://doi.org/10.1126/science.aba6853.
Wilson, M.J., 1999. The origin and formation of clay minerals in soils: past, present and future perspectives. Clay Mineralogy 34, 7–25. https://doi.org/10.1180/000985599545957.